PHYSICAL SCIENCES

3D DNA origami pincers that multitask on giant unilamellar vesicles

Pengfei Zhan[1,2]†, Juanjuan Yang[2,3]†, Longjiang Ding[2,3], Xinxin Jing[2,3], Katharina Hipp[4], Stephan Nussberger[5], Hao Yan[6], Na Liu[2,3]*

Proteins self-assemble to function in living cells. They may execute essential tasks in the form of monomers, complexes, or supramolecular cages via oligomerization, achieving a sophisticated balance between structural topology and functional dynamics. The modularity and programmability make DNA origami unique in mimicking these key features. Here, we demonstrate three-dimensional reconfigurable DNA origami pincers (DOPs) that multitask on giant unilamellar vesicles (GUVs). By programmably adjusting their pinching angle, the DOPs can dynamically control the degree of GUV remodeling. When oligomerized on the GUV to form origami cages, the DOP units interact with one another and undergo reorganization, resulting in the capture, compartmentalization, and detachment of lipid fragments. This oligomerization process is accompanied with membrane disruptions, enabling the passage of cargo across the membrane. We envisage that interfacing synthetic cells with engineered, multifunctional DNA nanostructures may help to confer customized cellular properties, unleashing the potential of both fields.

INTRODUCTION

Proteins participate in almost every process of cellular life. They maintain the cell shape, catalyze chemical reactions, regulate cargo transport, and coordinate cell signaling pathways (*1*). Intriguingly, protein subunits are often oligomerized into cage-like superstructures, which are strongly guided by symmetry (*2*). These so-called protein cages with diversified morphologies support critical cellular functions, providing the predominate means of building complexity in living systems (*3*). Although the working mechanisms of most proteins are beyond what scientists can now replicate, the enthusiasm to construct their synthetic equivalents with reduced complexity is everlasting (*4*, *5*). Such efforts may have great significance for the development of new biomaterials (*6*), nanomedicine (*7*), drug delivery (*8*), and vaccine (*9*) and for the fundamental understanding of the origin of life (*10*).

DNA nanotechnology has been used to create engineered structures that mimic the key features of biological systems (*11*–*18*). The success stems from the fact that DNA is a unique genetic and construction material. It affords versatile design and engineering capabilities, as well as enables highly specific and programmed tasks on the molecular level (*19*–*24*). Notably, DNA structures can be designed to work under user-defined interactions and environmental settings, usually impossible to achieve in complex biological systems (*25*–*28*). These capabilities have made DNA nanotechnology an important player in synthetic biology, especially providing a mechanistic framework to interact with synthetic cells (*29*–*32*). For instance, Franquelim *et al.* (*33*) constructed curved DNA origami inspired by BAR domain proteins to sculpt lipid membranes. Journot *et al.* (*34*) realized DNA triskelion networks that were reminiscent of clathrin-coated pits. Grome *et al.* (*35*) created dynamin mimics using DNA origami spirals to induce membrane tubulation. Furthermore, Birkholz *et al.* (*36*) demonstrated multifunctional DNA nanopores, which could puncture and remodel lipid membranes. In addition, tension-loaded DNA clamps were used to drive membrane tabulation and budding, providing insights into achieving spatiotemporal control over membrane dynamics (*37*).

Here, we demonstrate three-dimensional (3D) reconfigurable DNA origami pincers (DOPs) that multitask on giant unilamellar vesicles (GUVs) for dynamic GUV remodeling, capturing, compartmentalization, and subsequent detachment of lipid fragments from GUVs, as well as transport of molecules across the membrane by inducing transient pores (Fig. 1). In the monomer state, the membrane-bound DOPs can dynamically control the degree of the GUV morphological changes via programmably adjusting their pinching angle. When oligomerized on the GUV membrane, multiple DOP units interact with one another and self-assemble into origami cages with defined topology. During oligomerization, the reorganization of the DOP units disrupts the GUV membrane. Lipid fragments captured by the DOP units are compartmented by the origami cages and subsequently detached from the GUV. The oligomerization process induces the formation of transient membrane pores, enabling the passage of cargo across the membrane.

RESULTS

Programmable GUV remodeling by 3D reconfigurable DOPs

The 3D DOP has three interlinked origami bundles (~50 nm), each of which contains 14 DNA duplexes packed in a honeycomb lattice (Fig. 2A and fig. S1). The angle formed between the bundles is controlled by the segment of the single-stranded DNA (ssDNA) scaffold, which passes twice through them (*38*). In the relaxed state, the three bundles are flexible. By adding respective locking strands L120, L90, L60, or L30, the length of this segment can be altered through toehold-mediated strand displacement reactions, so that the bundles can be tightened to establish a defined pinching angle $\theta = 120°$, 90°, 60°, or 30° (Fig. 2A and figs. S1 to S4). The corresponding transmission electron microscopy (TEM) images of the DOPs at different θ states and in the relaxed state after the gel purification are presented

[1]Hangzhou Institute of Medicine, Chinese Academy of Sciences, 310022 Hangzhou, Zhejiang, China. [2]2nd Physics Institute, University of Stuttgart, D-70569 Stuttgart, Germany. [3]Max Planck Institute for Solid State Research, D-70569 Stuttgart, Germany. [4]Electron Microscopy, Max Planck Institute for Biology Tübingen, 72076 Tübingen, Germany. [5]Department of Biophysics, Institute of Biomaterials and Biomolecular Systems, University of Stuttgart, D-70569 Stuttgart, Germany. [6]Biodesign Center for Molecular Design and Biomimetics, Arizona State University, Tempe, AZ 85287, USA.
*Corresponding author. Email: na.liu@pi2.uni-stuttgart.de
†These authors contributed equally to this work.

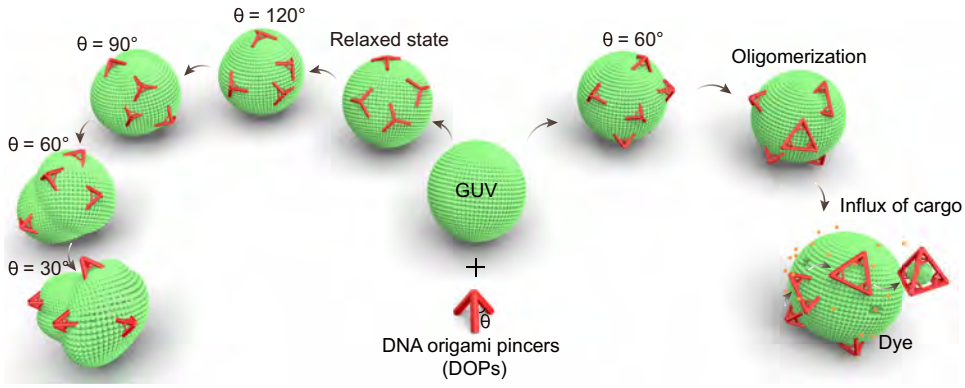

Fig. 1. Schematic of 3D DOPs that multitask on GUVs. The red structures represent DNA origami pincers (DOPs), and the green vesicles represent giant unilamellar vesicles (GUVs). The reconfigurable DOPs can remodel the GUV morphology in a programmable manner by changing the pinching angle θ. Oligomerization of the DOPs on the GUV leads to the capture, compartmentalization, and detachment of lipid fragments, as well as the formation of transient membrane pores for cargo transport across the membrane. Note that the schematic provides a hypothetical representation, in which the DOPs and GUVs are not depicted to scale.

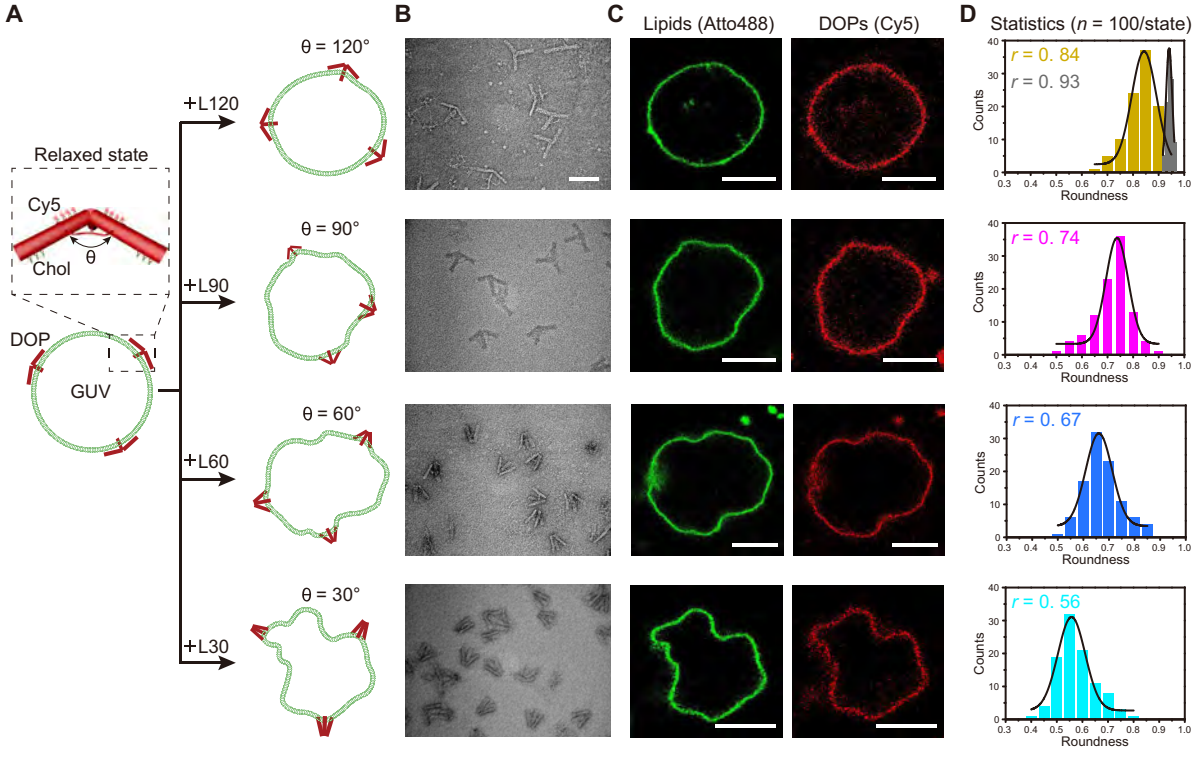

Fig. 2. Programmable GUV remodeling by 3D reconfigurable DOPs. (**A**) Schematic of the DOPs transiting from the relaxed state to different θ states by the addition of corresponding locking strands (L120, L90, L60, or L30) to control the degree of GUV remodeling. Note that the DOPs and GUVs are not depicted to scale. (**B**) Transmission electron microscopy (TEM) images of the DOPs at different θ states (120°, 90°, 60°, or 30°). Scale bar, 100 nm. (**C**) Confocal fluorescence microscopy images of the GUVs, when the DOPs are at different θ states. Scale bars, 5 μm. (**D**) Roundness distributions of the DOP-bound GUVs at different θ states. *r* represents the fitted population peak value.

in Fig. 2B and fig. S5, respectively. To enable confocal fluorescence microscopy, the DOP is labeled with 12 Cyanine5 (Cy5) dyes on its exterior, four on each bundle (Fig. 2A and fig. S6). For membrane binding, nine cholesterol-tagged ssDNA handles are extended from its interior, three on each bundle. Fewer cholesterol anchors result in a lower membrane affinity of the DOPs (fig. S6). The influence of the DOP concentration on membrane binding is also investigated (fig. S7). A DOP concentration of 2.5 nM, which does not introduce evident GUV deformations, is adopted in the following experiments.

The DOPs in the relaxed state are first incubated with GUVs [1,2-dioleoyl-*sn*-glycero-3-phosphocholine (DOPC) and 0.5% 1,2-dioleoyl-*sn*-glycero-3-phosphoethanolamine–Atto488 (Atto488-DOPE)] at room temperature. At equilibrium (~1 hour), the mixture is divided into four equivalent samples. Locking strands L120, L90, L60, or L30 (0.5 μl, 200 μM each; table S1) are added into the

respective samples to reconfigure the DOPs to θ = 120°, 90°, 60°, or 30° state accordingly. After incubation at 40° for 1 hour under the isosmotic condition, the samples are characterized by confocal fluorescence microscopy (figs. S8 to S11). The DOP surface density σ at each angle state is presented in table S2. As shown in Fig. 2C, the fluorescence signals of the lipids and the DOPs at different θ states colocalize, confirming the successful binding of the DNA structures on the GUV membranes. In addition, the degree of GUV remodeling is intimately dependent on the pinching angle θ. Specifically, the smaller the θ, the stronger deformations the GUVs exhibit.

To quantitatively dissect the correlation between deformations and the pinching angle θ, the roundness (*r*), which measures how closely an object's shape approaches that of a perfect circle (*r* = 1.0), is calculated from 100 GUVs for each θ state (Fig. 2D). In the relaxed state, the population peak (fitted mean value) is centered around *r* = 0.93, revealing that no evident GUV morphological changes are present. When θ is locked to 120°, the distribution profile is broadened and *r* shifts to 0.84. This demonstrates that the pinching action executed by the DOPs can induce membrane deformations. When the pinching is further strengthened by fastening the DOPs to smaller θ states, membrane deformations become more and more prominent. *r* eventually decreases to 0.56 at θ = 30°. As a control, by the addition of nonspecific DNA strands, no obvious GUV remodeling is observed (fig. S12). It is hypothetical that the membrane-bound DOPs can effectively sculpt the GUV morphology by facile control over their pinching angle θ. It signifies that the conformation changes of the DOPs at the nanoscale can be directly transduced to the morphological changes of GUVs at the microscale.

To further explore the programmability of GUV remodeling, the DOPs are dynamically reconfigured on GUVs among multiple θ states. After the DOPs transit from the relaxed state to θ = 90° state (Fig. 3A), releasing strands (R90) and locking strands (L30) are added into the sample. While the former releases L90 from the DOPs through toehold-mediated strand displacement reactions, the latter locks the DOPs to θ = 30° state. As evidenced in Fig. 3B and fig. S13, by successively tightening the DOPs, *r* decreases from 0.93 (relaxed state) to 0.75 (θ = 90°) and to 0.66 (θ = 30°). Alternatively, if the DOPs are first locked to θ = 30° and then loosened to θ = 90° (Fig. 3C and fig. S14), then *r* first decreases from 0.93 to 0.56, followed by an increase to 0.67. In other words, the degree of GUV remodeling can be recovered in a controlled manner. Particular emphasis is placed on the comparison between the statistical results in Figs. 2 and 3. With one step of reconfiguration from the relaxed state to θ = 90° state, *r* is 0.74 (Fig. 2C) and 0.75 (Fig. 3B), respectively, while, from the relaxed state to θ = 30° state, *r* shifts to 0.56 in both cases (Figs. 2C and 3D). After the second step of reconfiguration from θ = 90° state to θ = 30° state, *r* changes to 0.66 (Fig. 3B). However, the direct route from the relaxed state to θ = 30° state yields *r* = 0.56 (Figs. 2C and 3D). Similarly, after the second step of

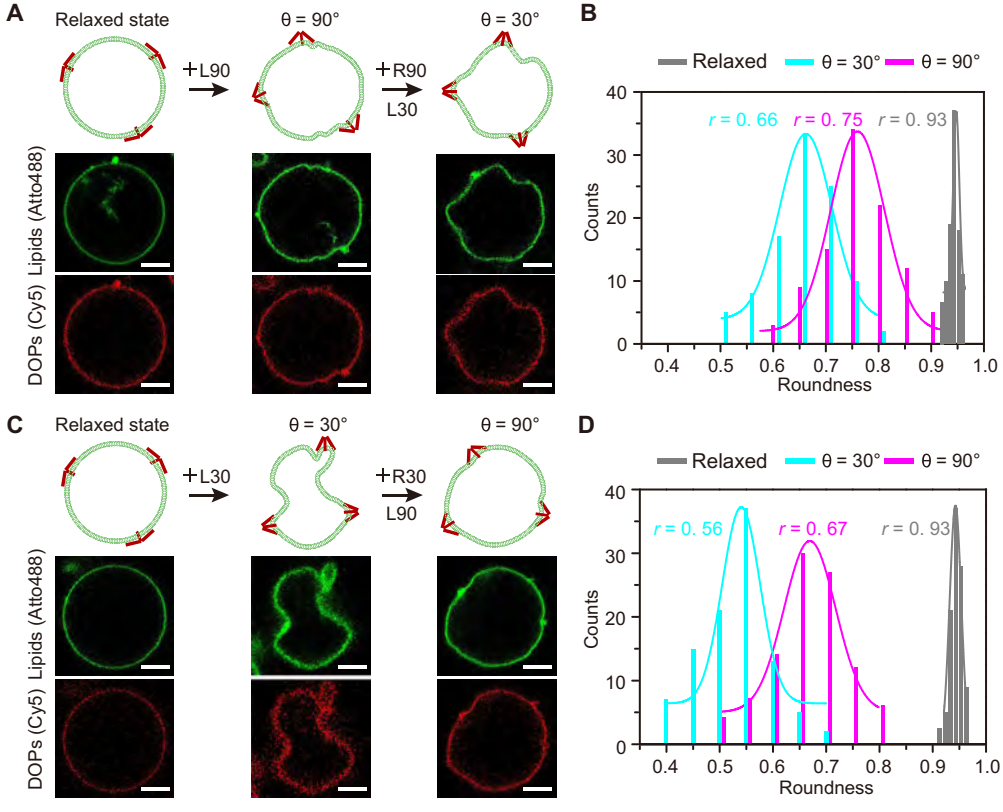

Fig. 3. Reconfiguration of DOPs among multiple θ states on GUVs. (**A**) Confocal fluorescence microscopy images of the DOP-bound GUVs for the transition of the DOPs from the relaxed state, to θ = 90°, and then to θ = 30°. Scale bars, 2 μm. (**B**) Roundness distribution of the DOP-bound GUVs for the transition of the DOPs from the relaxed state, to θ = 90°, and then to θ = 30°. (**C**) Confocal fluorescence microscopy images of the DOP-bound GUVs for the transition of the DOPs from the relaxed state, to θ = 30°, and then to θ = 90°. Scale bars, 2 μm. (**D**) Roundness distribution of the DOP-bound GUVs for the transition of the DOPs from the relaxed state, to θ = 30°, and then to θ = 90°.

reconfiguration from θ = 30° state to θ = 90°, *r* only increases to 0.67 (Fig. 3D) instead of 0.74 (Fig. 2C). It elucidates that multiple steps of operations introduce a slight performance degradation (figs. S15 and S16), which could be improved using optimized toehold designs or other external stimuli (*39*, *40*).

Oligomerization of DOPs and formation of transient membrane pores

Next, we set out to investigate the formation of origami cages by oligomerization of the DOPs on GUVs (Fig. 4A). The ends of the DOP bundles are specifically designed, so that multiple DOP units can be connected together upon the addition of DNA linkers (*41*–*43*). The topology of the formed origami cages is determined by θ. With θ = 60°, four DOP units can self-assemble into a tetrahedron (Fig. 4A). After incubation of the DOPs (θ = 60°) with GUVs, no marked membrane deformations are visible (Fig. 4B). This is in contrast to the substantial GUV remodeling (*r* = 0.67) observed in Fig. 2, in which the DOPs are reconfigured from the relaxed state to θ = 60° state directly on GUVs. It highlights the close relationship between the dynamic pinching action of the DOPs and the dynamic remodeling of the GUV morphology.

Taking one step further, Cy3 (5 μM) dyes are added into the sample, filling the exterior space of the GUVs (initial state, Fig. 4B). Upon the addition of the DNA linkers, the normalized fluorescence intensity difference $(\langle I_{out}\rangle - \langle I_{in}\rangle)/\langle I_{out}\rangle$ of the GUVs is monitored over time using confocal fluorescence microscopy (Fig. 4C and movie S1). Fluorescence signals in the GUV interior are detected within several minutes. The passage of the Cy3 molecules across the membrane suggests the formation of transmembrane pores during the DOP oligomerization. The influx reaches an equilibrium around 1 hour, leading to a homogeneous distribution of Cy3 within the GUV lumen at the final state (Fig. 4, B and C). Alternatively, no cargo influx is observed by adding nonspecific DNA strands of the same amount (fig. S17) or linkers that form dimers (fig. S18). The statistical result of $(\langle I_{out}\rangle - \langle I_{in}\rangle)/\langle I_{out}\rangle$ based on $n = 130$ GUVs per initial/final state corroborates the effective molecular transport across the membrane during the DOP oligomerization (Fig. 4D).

To understand the relationship between the DOP oligomerization and the transmembrane pore formation, fluorescence recovery after photobleaching (FRAP) measurements are carried out on single GUVs bound with DOPs (θ = 60°) at different times after the addition of the DNA linkers. After 1 hour of oligomerization (Fig. 5A), the transported Cy3 molecules are homogeneously dispersed in the GUV interior. Photobleaching of Cy3 within the GUV using FRAP leads to an immediate fluorescence intensity drop, followed by a gradual signal recovery to almost the original value in 20 min (pink curve in Fig. 5B). After 1.5 or 2 hours of oligomerization, the fluorescence intensity recovers much slower and achieves a signal plateau in 30 min (orange curve) or 45 min (blue curve), which is lower than the original value (figs. S19 and S20). With oligomerization overnight, the fluorescence intensity can no longer recover (green curve in Fig. 5B and fig. S21). As a control, the DOP oligomerization in the absence of GUVs is also carried out. It shows that, after adding the DNA linkers, origami tetrahedrons start to partially form in 10 min and become more and more intact over time (fig. S22). This set of experiments extrapolates that the DOP oligomerization process is accompanied by the formation of transient pores, which allow transport of Cy3 across the membrane. The influx of Cy3 persists, until the oligomerization completes. Afterward, the membrane pores are likely sealed, inhibiting further transport of cargo. We also carry out the experiment by adding fully formed tetrahedrons as a control. The experimental results show that no influx is observed in this case, indicating the absence of membrane pores (fig. S23). To evaluate the pore size, a set of influx assays is conducted using Cy3 and fluorescein isothiocyanate (FITC)–dextran of varying molecular weights as optical probes. As shown in fig. S24, the formed pores allow a complete passage of Cy3 (600 Da) across the membrane, whereas they show partial permeability to 3-kDa FITC-dextran

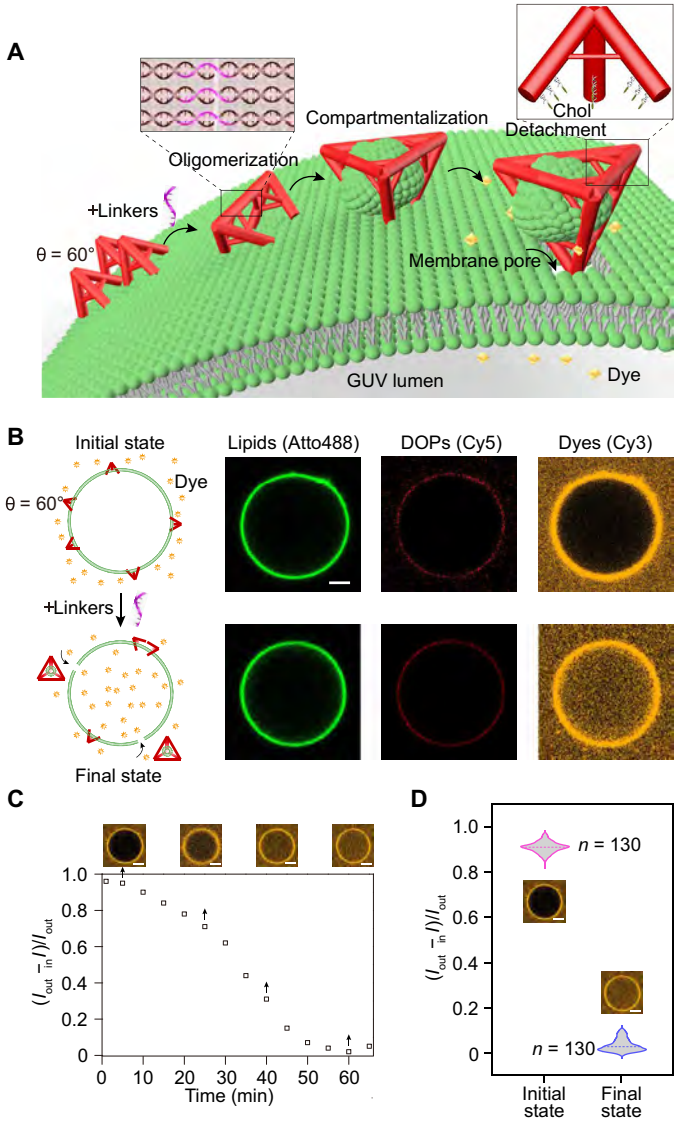

Fig. 4. Oligomerization of the DOP units and formation of transient membrane pores. (**A**) Schematic of oligomerization of the DOPs (θ = 60°) and formation of transient membrane pores for cargo transport. Note that the schematic provides a hypothetical representation, in which the DOPs and GUVs are not depicted to scale. (**B**) Transport of dyes (Cy3) across the GUV membrane through transient pores, resulting from oligomerization of the DOPs by the addition of the DNA linkers. Scale bar, 1 μm. (**C**) Time course of the dye influx and corresponding confocal fluorescence images at specific times. Scale bars, 2 μm. (**D**) Statistical data of the dye influx at the initial and final states, respectively. Scale bars, 2 μm.

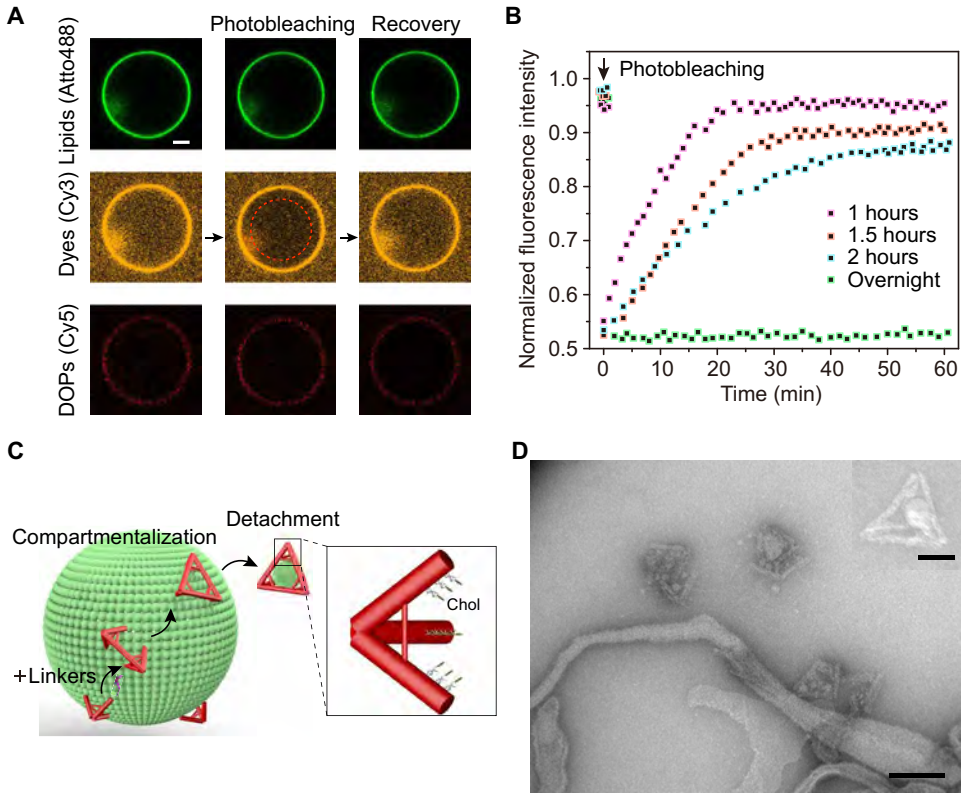

Fig. 5. Compartmentalization, detachment, and transmembrane cargo transport. (**A**) Photobleaching of Cy3 dyes within the GUV, after 1 hour of oligomerization of the DOPs (θ = 60°). Scale bar, 2 μm. (**B**) Normalized fluorescence intensities using FRAP after different oligomerization times: 1 hour, 1.5 hours, 2 hours, and overnight. (**C**) Schematic of compartmentalization and detachment of lipid fragments by the DOP oligomerization. Note that the schematic provides a hypothetical representation, in which the DOPs and GUVs are not depicted to scale. (**D**) TEM image of the GUV membranes and oligomerized DOPs. Scale bar, 300 nm. Inset: Compartmentalization of lipid fragments by a DOP tetrahedron. Scale bar, 50 nm.

(~3.4 nm) (*18*, *44*). The permeability further decreases in the case of 10-kDa FITC-dextran (~6.0 nm) and becomes negligible in the case of 40-kDa FITC-dextran (~11.6 nm). We therefore estimate the average size of the formed pores is below 10 nm.

Compartmentalization, detachment, and transmembrane cargo transport

To uncover the nature of the transient pores, we conduct TEM imaging of the samples after oligomerization overnight from Fig. 5B. Compartmentalization of lipid fragments by intact or partial origami tetrahedrons is observed (Fig. 5D and fig. S25). The DOP units with cholesterol-tagged bundles are bound to the membrane. During oligomerization, the DOP units reorganize on the GUV for interconnection among themselves to form origami cages (Fig. 5C). The reorganization induces surface tension and membrane disruptions, resulting in transient membrane porations and compartmentalization of lipid fragments by the origami cages. The lipid-containing origami cages are subsequently detached from the GUV. Such membrane disruptions continue, allowing for the passage of Cy3, until the oligomerization process and the accompanied cage detachment completely cease. With the closure of the transient pores, influx of cargo is no longer permitted. Therefore, after photobleaching, the fluorescence signals cannot be recovered in the case of oligomerization overnight (green curve in Fig. 5B).

DISCUSSION

In this work, we have demonstrated that the 3D reconfigurable DOP monomers can work together to regulate the morphological changes of GUVs in a programmable manner. Furthermore, the DOP units can interconnect and self-assemble into origami cages to achieve both defined topology and functional dynamics on GUVs. The DOP oligomerization on the GUV induces transient membrane pores, which allow for the influx of cargo. We envision that, by interfacing cells with engineered dynamic DNA nanostructures, it may foster tantalizing opportunities to interrogate interesting biological questions in the future (*45*). For instance, by building synthetic equivalents of proteins, one can grasp the basic relation between the structure and function of proteins in cells, as well as understand when, where, and how proteins occur to function, at least to some extent. In addition, given the ease of engineering from the bottom-up, one can harness the simplicity of DNA origami to create complexity by building artificial systems with nonnatural functionalities. For instance, taking its ability to position bioactive moieties at the nanoscale, the exterior surface, the interior surface, and the interface between the origami units can be versatility modified with customer-defined properties, so that the self-assembled high-order architectures (e.g., interconnection of units into cages and interconnection of cages into cage chains or lattices) may synergistically combine the functions of several protein families, which work independently in biological cells. Closely related to our work, Dietz and Pinner (*46*)

have recently used DNA origami shells on vesicles to induce membrane budding and mediate scission, opening avenues for the exploration of membrane mechanics. Despite the limited cognition of biological systems as of today, the efforts along this line will add scientific breath for a deeper understanding of cellular life.

MATERIALS AND METHODS

Design, folding, and purification of DOPs

All the DNA structures were designed using caDNAno v.0.2 (*47*) and the DNA sequences are provided in table S1. The DNA strands and the DNA conjugate strands were purchased from Sigma-Aldrich and Integrated DNA Technologies, respectively. The DOPs were prepared as follows. The folding reaction mixture contained scaffolds of 30 nM and oligonucleotide strands of 300 nM in a tris-EDTA (TE)/Mg^{2+} buffer [10 mM tris, 1 mM EDTA, 18 mM $MgCl_2$, and 5 mM NaCl (pH 8)]. A 100-μl solution was annealed using a thermocycler (Eppendorf) by heating the solution to 90°C and cooling it to 25°C at a constant rate of 0.18°C min^{-1} for 24 hours. Then, the mixture was loaded into a 1.5% agarose gel with 0.5× TBE (45 mM tris base, 45 mM boric acid, and 1 mM EDTA) and 10 mM $MgCl_2$ for 2 hours at 5 V/cm. After the image analysis using a Bio-Rad imager, the fractions containing well-formed monomeric DOPs were combined and concentrated using PEG fractionation. The pellet was then dissolved in a TE buffer containing 12.5 mM $MgCl_2$ and stored at 4°C. Before incubating with GUVs, cholesterol-modified DNA strands and the purified DOPs were mixed with a ratio of 2:1 for 2 hours at room temperature.

Preparation of GUVs

Chloroform stock solutions of DOPC (18:1; Avanti Polar Lipids) and Atto488-DOPE (AttoTEC) were mixed at a ratio of 99.5%:0.5% to yield a 5 mM stock solution. The stock solution (30 μl) was put onto indium tin oxide (ITO) slides, dried, and desiccated for 20 min. Afterward, the ITO slides were placed into an electroformation chamber with 270 μl of 210 mosmol sucrose solution. GUVs were electroformed using a Vesicle Prep Pro device from Nanion. An ac electric field with an amplitude of 3 V and a frequency of 5 Hz was applied at 37°C for 2 hours.

Confocal fluorescence microscopy

Ten microliters of bovine serum albumin (BSA; 2 mg/ml) was added into a 200-μl chamber (ibidi). After 20 min, the chamber was washed with an incubation buffer [25 mM Hepes-KOH, 100 mM KCl, and 10 mM $MgCl_2$ (pH 7.4)]. Ten microliters of the GUV stock and 10 μL of the cholesterol-modified DOPs (50 nM) were mixed in 180 μl of the incubation buffer for 1 hour. The mixture was then dispensed on the BSA-coated glass and allowed for the GUV sedimentation on the glass surface for 20 min. To actuate the DOPs for membrane remodeling, 1.5 μl (L30), 3 μl (L60), 4.5 μl (L90), or 6 μl (L120) (200 μM each; dissolved in double deionized water) was added into the chamber and incubated for 1 hour at 40°C in each case (see table S1). Alternatively, the same amount of nonspecific DNA oligonucleotides was added as a negative control. The roundedness was calculated using MATLAB, following a standard protocol (www.mathworks.com/help/images/identifying-round-objects.html). To prepare the dye influx assay, 3 μl of Cy3 dyes (30 μM) were added to the mixture before being loaded into the chamber. Three microliters of the linker strands were added to the DOP-bound GUVs and incubated for 1 hour at 40°C.

Fluorescence recovery after photobleaching

For the FRAP experiments, the equatorial plane of the GUV was chosen. Six images were acquired before the region of interest (ROI) was illuminated for 90 iterations at the 100% laser power at 565 nm (for Cy3). Then, the ROI was monitored for up to 60 min to track the recovery of the fluorescence.

TEM characterization

For TEM imaging, 10 μl of 1 nM DOPs were deposited on freshly glow-discharged carbon/formvar TEM grids. Before depositing the DNA structure solution, the grids were treated by negative glow discharge for 1 min. After 10 min of deposition, the grids were treated with a uranyl formate solution (2%) for 15 s.

Supplementary Materials

The PDF file includes:

Figs. S1 to S25
Tables S1 and S2
Legend for movie S1
Legend for data S1
References

Other Supplementary Material for this manuscript includes the following:

Movie S1
Data S1

REFERENCES AND NOTES

1. A. E. Todd, C. A. Orengo, J. M. Thornton, Evolution of function in protein superfamilies, from a structural perspective. *J. Mol. Biol.* **307**, 1113–1143 (2001).
2. W. M. Aumiller, M. Uchida, T. Douglas, Protein cage assembly across multiple length scales. *Chem. Soc. Rev.* **47**, 3433–3469 (2018).
3. H. T. McMahon, E. Boucrot, Molecular mechanism and physiological functions of clathrin-mediated endocytosis. *Nat. Rev. Mol. Cell Biol.* **12**, 517–533 (2011).
4. J. Zhu, N. Avakyan, A. Kakkis, A. M. Hoffnagle, K. Han, Y. Li, Z. Zhang, T. S. Choi, Y. Na, C.-J. Yu, Protein assembly by design. *Chem. Rev.* **121**, 13701–13796 (2021).
5. C. Lv, X. Zhang, Y. Liu, T. Zhang, H. Chen, J. Zang, B. Zheng, G. Zhao, Redesign of protein nanocages: The way from 0D, 1D, 2D to 3D assembly. *Chem. Soc. Rev.* **50**, 3957–3989 (2021).
6. L. Li, G. Chen, Precise assembly of proteins and carbohydrates for next-generation biomaterials. *J. Am. Chem. Soc.* **144**, 16232–16251 (2022).
7. Q. Zhang, J. Zhang, J. Song, Y. Liu, X. Ren, Y. Zhao, Protein-based nanomedicine for therapeutic benefits of cancer. *ACS Nano* **15**, 8001–8038 (2021).
8. E. Kianfar, Protein nanoparticles in drug delivery: Animal protein, plant proteins and protein cages, albumin nanoparticles. *J. Nanobiotechnol.* **19**, 159 (2021).
9. M. S. Gebre, L. A. Brito, L. H. Tostanoski, D. K. Edwards, A. Carfi, D. H. Barouch, Novel approaches for vaccine development. *Cell* **184**, 1589–1603 (2021).
10. T. G. Edwardson, M. D. Levasseur, S. Tetter, A. Steinauer, M. Hori, D. Hilvert, Protein cages: From fundamentals to advanced applications. *Chem. Rev.* **122**, 9145–9197 (2022).
11. N. C. Seeman, H. F. Sleiman, DNA nanotechnology. *Nat. Rev. Mater.* **3**, 17068 (2018).
12. P. Zhan, K. Jahnke, N. Liu, K. Göpfrich, Functional DNA-based cytoskeletons for synthetic cells. *Nat. Chem.* **14**, 958–963 (2022).
13. S. Sethi, H. Sugiyama, M. Endo, Biomimetic DNA nanotechnology to understand and control cellular responses. *Chembiochem* **23**, e202100446 (2022).
14. Z. Huang, L. Qiu, T. Zhang, W. Tan, Integrating DNA nanotechnology with aptamers for biological and biomedical applications. *Matter* **4**, 461–489 (2021).
15. N. Arulkumaran, M. Singer, S. Howorka, J. R. Burns, Creating complex protocells and prototissues using simple DNA building blocks. *Nat. Commun.* **14**, 1314 (2023).
16. S. Agarwal, M. A. Klocke, P. E. Pungchai, E. Franco, Dynamic self-assembly of compartmentalized DNA nanotubes. *Nat. Commun.* **12**, 3557 (2021).
17. Y. Xing, A. Dorey, L. Jayasinghe, S. Howorka, Highly shape- and size-tunable membrane nanopores made with DNA. *Nat. Nanotechnol.* **17**, 708–713 (2022).
18. A. Fragasso, N. De Franceschi, P. Stömmer, E. O. Van Der Sluis, H. Dietz, C. Dekker, Reconstitution of ultrawide DNA origami pores in liposomes for transmembrane transport of macromolecules. *ACS Nano* **15**, 12768–12779 (2021).
19. Y. Hu, C. M. Niemeyer, From DNA nanotechnology to material systems engineering. *Adv. Mater.* **31**, e1806294 (2019).

20. E. Del Grosso, E. Franco, L. J. Prins, F. Ricci, Dissipative DNA nanotechnology. *Nat. Chem.* **14**, 600–613 (2022).
21. S. Dey, C. Fan, K. V. Gothelf, J. Li, C. Lin, L. Liu, N. Liu, M. A. Nijenhuis, B. Saccà, F. C. Simmel, H. Yan, P. Zhan, DNA origami. *Nat. Rev. Methods Primers* **1**, 13 (2021).
22. C.-M. Huang, A. Kucinic, J. A. Johnson, H.-J. Su, C. E. Castro, Integrated computer-aided engineering and design for DNA assemblies. *Nat. Mater.* **20**, 1264–1271 (2021).
23. X. Shi, A.-K. Pumm, C. Maffeo, F. Kohler, E. Feigl, W. Zhao, D. Verschueren, R. Golestanian, A. Aksimentiev, H. Dietz, C. Dekker, A DNA turbine powered by a transmembrane potential across a nanopore. *Nat. Nanotechnol.* **19**, 338–344 (2024).
24. R. P. Thomsen, M. G. Malle, A. H. Okholm, S. Krishnan, S. S.-R. Bohr, R. S. Sørensen, O. Ries, S. Vogel, F. C. Simmel, N. S. Hatzakis, J. Kjems, A large size-selective DNA nanopore with sensing applications. *Nat. Commun.* **10**, 5655 (2019).
25. G. A. Knappe, E.-C. Wamhoff, M. Bathe, Functionalizing DNA origami to investigate and interact with biological systems. *Nat. Rev. Mater.* **8**, 123–138 (2023).
26. S. Jia, S. C. Phua, Y. Nihongaki, Y. Li, M. Pacella, Y. Li, A. M. Mohammed, S. Sun, T. Inoue, R. Schulman, Growth and site-specific organization of micron-scale biomolecular devices on living mammalian cells. *Nat. Commun.* **12**, 5729 (2021).
27. H. Ijäs, I. Hakaste, B. Shen, M. A. Kostiainen, V. Linko, Reconfigurable DNA origami nanocapsule for pH-controlled encapsulation and display of cargo. *ACS Nano* **13**, 5959–5967 (2019).
28. Y. Li, C. Maffeo, H. Joshi, A. Aksimentiev, B. Ménard, R. Schulman, Leakless end-to-end transport of small molecules through micron-length DNA nanochannels. *Sci. Adv.* **8**, eabq4834 (2022).
29. D. Di Iorio, S. V. Wegner, Towards applications of synthetic cells in nanotechnology. *Curr. Opin. Chem. Biol.* **68**, 102145 (2022).
30. M. Fletcher, J. Zhu, R. Rubio-Sánchez, S. E. Sandler, K. A. Nahas, L. D. Michele, U. F. Keyser, R. Tivony, DNA-based optical quantification of ion transport across giant vesicles. *ACS Nano* **16**, 17128–17138 (2022).
31. W. Wang, P. R. Hayes, X. Ren, R. E. Taylor, Synthetic cell armor made of DNA origami. *Nano Lett.* **23**, 7076–7085 (2023).
32. N. Yamashita, Y. Sato, Y. Suzuki, D. Ishikawa, M. Takinoue, DNA-origami-armored DNA condensates. ChemRxiv (2024); https://doi.org/10.26434/chemrxiv-2024-njhv3.
33. H. G. Franquelim, A. Khmelinskaia, J.-P. Sobczak, H. Dietz, P. Schwille, Membrane sculpting by curved DNA origami scaffolds. *Nat. Commun.* **9**, 811 (2018).
34. C. M. A. Journot, V. Ramakrishna, M. I. Wallace, A. J. Turberfield, Modifying membrane morphology and interactions with DNA origami clathrin-mimic networks. *ACS Nano* **13**, 9973–9979 (2019).
35. M. W. Grome, Z. Zhang, F. Pincet, C. Lin, Vesicle tubulation with self-assembling DNA nanosprings. *Angew. Chem. Int. Ed. Engl.* **57**, 5330–5334 (2018).
36. O. Birkholz, J. R. Burns, C. P. Richter, O. E. Psathaki, S. Howorka, J. Piehler, Multi-functional DNA nanostructures that puncture and remodel lipid membranes into hybrid materials. *Nat. Commun.* **9**, 1521 (2018).
37. L. Liu, Q. Xiong, C. Xie, F. Pincet, C. J. S. A. Lin, Actuating tension-loaded DNA clamps drives membrane tubulation. *Sci. Adv.* **8**, eadd1830 (2022).
38. P. Zhan, P. K. Dutta, P. Wang, G. Song, M. Dai, S.-X. Zhao, Z.-G. Wang, P. Yin, W. Zhang, B. Ding, Y. Ke, Reconfigurable three-dimensional gold nanorod plasmonic nanostructures organized on DNA origami tripod. *ACS Nano* **11**, 1172–1179 (2017).
39. H. Ramezani, H. Dietz, Building machines with DNA molecules. *Nat. Rev. Genet.* **21**, 5–26 (2020).
40. V. Maingi, Z. Zhang, C. Thachuk, N. Sarraf, E. R. Chapman, P. W. Rothemund, Digital nanoreactors to control absolute stoichiometry and spatiotemporal behavior of DNA receptors within lipid bilayers. *Nat. Commun.* **14**, 1532 (2023).
41. A. Monferrer, J. A. Kretzmann, C. Sigl, P. Sapelza, A. Liedl, B. Wittmann, H. Dietz, Broad-spectrum virus trapping with heparan sulfate-modified DNA origami shells. *ACS Nano* **16**, 20002–20009 (2022).
42. C. Sigl, E. M. Willner, W. Engelen, J. A. Kretzmann, K. Sachenbacher, A. Liedl, F. Kolbe, F. Wilsch, S. A. Aghvami, U. Protzer, M. F. Hagan, S. Fraden, H. Dietz, Programmable icosahedral shell system for virus trapping. *Nat. Mater.* **20**, 1281–1289 (2021).
43. R. Iinuma, Y. Ke, R. Jungmann, T. Schlichthaerle, J. B. Woehrstein, P. Yin, Polyhedra self-assembled from DNA tripods and characterized with 3D DNA-PAINT. *Science* **344**, 65–69 (2014).
44. R. Hanselmann, W. Burchard, R. Lemmes, D. Schwengers, Characterization of DEAE-dextran by means of light scattering and combined size-exclusion chromatography/low-angle laser light scattering/viscometry. *Macromol. Chem. Phys.* **196**, 2259–2275 (1995).
45. H. F. Lodish, *Molecular Cell Biology* (W. H. Freeman & Co., ed. 6, 2007).
46. H. Dietz, M. T. Pinner, Programmable DNA shell scaffolds for directional membrane budding. *bioRxiv* 2024.01.18.576181 (2024).
47. S. M. Douglas, A. H. Marblestone, S. Teerapittayanon, A. Vazquez, G. M. Church, W. M. Shih, Rapid prototyping of 3D DNA-origami shapes with caDNAno. *Nucleic Acids Res.* **37**, 5001–5006 (2009).
48. A. Czogalla, D. J. Kauert, H. G. Franquelim, V. Uzunova, Y. Zhang, R. Seidel, P. Schwille, Amphipathic DNA origami nanoparticles to scaffold and deform lipid membrane vesicles. *Angew. Chem. Int. Ed. Engl.* **54**, 6501–6505 (2015).
49. A. Czogalla, D. J. Kauert, R. Seidel, P. Schwille, E. P. Petrov, DNA origami nanoneedles on freestanding lipid membranes as a tool to observe isotropic–nematic transition in two dimensions. *Nano Lett.* **15**, 649–655 (2015).
50. A. Khmelinskaia, H. G. Franquelim, E. P. Petrov, P. Schwille, Effect of anchor positioning on binding and diffusion of elongated 3D DNA nanostructures on lipid membranes. *J. Phys. D Appl. Phys.* **49**, 194001 (2016).

Acknowledgments: We acknowledge the Technology Platform "Cellular Analytics" of the Stuttgart Research Center Systems Biology for support and assistance in this work. We thank S. Eisler for the assistance with confocal microscopy. **Funding:** This project was financed by the Baden-Württemberg Stiftung (Internationale Spitzenforschung, BWST-ISF2020-19). N.L. also acknowledges support from the Max Planck Society (Max Planck Fellow). **Author contributions:** N.L. and P.Z. conceived the study. P.Z. performed the experiments and data analysis. J.Y. prepared the GUVs. L.D. and X.J. helped with the TEM sample preparation. K.H. conducted the TEM characterization. S.N. and H.Y. provided helpful advice. N.L. supervised the project. N.L. and P.Z. wrote the manuscript with contributions from all authors. **Competing interests:** The authors declare that they have no competing interests. **Data and materials availability:** All data needed to evaluate the conclusions in the paper are present in the paper and/or the Supplementary Materials.

Submitted 5 January 2024
Accepted 10 July 2024
Published 16 August 2024
10.1126/sciadv.adn8903